

# The design and construction of the MICE Electron-Muon Ranger

May 10, 2016

## Abstract

The Electron-Muon Ranger (EMR) is a totally active scintillator detector installed in the beam of the Muon Ionization Cooling Experiment (MICE) [1]. The experiment will demonstrate ionization cooling, an essential technology needed for the realization of a Neutrino Factory and/or Muon Collider. The EMR is aimed at measuring the properties of the low energy beam composed of muons, electrons and pions, performing the identification particle by particle. The detector is made of 48 stacked layers alternately measuring  $X$  and  $Y$  coordinates. Each layer consists of 59 triangular scintillator bars. The read-out is based on FPGA custom made electronics and commercially available modules. This article will describe the construction of the detector, starting with the design of the detector up to its final commissioning with particle beam.

## 1 Introduction

### 1.1 Ionization cooling

The Neutrino Factory based on a high-energy muon storage-ring is the ultimate tool to study the neutrino mixing matrix and is established as the best facility to discover, and study the possible leptonic CP violation. It will produce the most intense, pure and focused neutrino beam ever achieved and is also the first step towards a  $\mu^+\mu^-$  collider. The Neutrino Factory accelerator complex will use as a sources muons, produced as a tertiary beam. A proton beam bombarding a target will produce pions. These pions will be captured and focused in a high-field solenoid channel and will decay to muons, creating a low energy muon beam with very large emittance. The emittance of the muons needs to be reduced, i.e the muon must be cooled, so that the beam can be accelerated efficiently.



Figure 1: Ionization cooling principle: 1. Energy loss by ionization ( $dE/dx$  reduces  $P_L$  and  $p_T$ ) 2. Heating from multiple scattering 3.  $P_L$  restored by RF cavities

Ionization cooling [2] (Fig. 1) provides the only practical solution to this problem, because it is fast enough to cool the beam within the muon lifetime ( $\tau_\mu \sim 2.2 \mu s$ ). The cooling effect is accomplished by passing the muons through a low-Z material (“absorber”), in which they loses energy via ionization, reducing both the longitudinal and the transverse components of the momentum. Later the longitudinal momentum is restored by accelerating cavities. The net effect is a reduction

of the beam emittance. To maximize cooling we need the absorber to be placed at a position where  
30 the transverse momentum  $P_T$  has a maximum (the transverse betatron function  $\beta_\perp$  has a minimum).

## 1.2 MICE

The international Muon Ionization Cooling Experiment (MICE) [1] is under development at the Rutherford Appleton Laboratory (UK). The goal of the experiment is to build a section of a cooling channel that can demonstrate the principle of Ionization cooling and to verify its performance in a  
35 muon beam.

Since energy loss by ionization and multiple Coulomb scattering are momentum dependent, the ionization cooling effect is momentum dependent. MICE (Fig. 2) uses variety of muon beams of limited intensity, having central momenta in the range  $140 - 240 \text{ MeV}/c$  and a momentum spread of  $\sim 20 \text{ MeV}/c$ . These muon beams are generated using a titanium target [3] which is dipped into the  
40 ISIS proton beam [4]. Produced secondary and tertiary particles are captured, momentum-selected and transported to the cooling section by a system of magnets which includes: 5 T superconducting pion decay solenoid, two dipole magnets, nine quadrupole magnets and a mechanism for inflation of the initial emittance called Diffuser.

The cooling section of MICE, is similar to the cooling channel for the International Design  
45 Study for the Neutrino Factory [5]. It consists of one primary lithium-hydride (LiH) absorber, two secondary absorbers, two focus coils and two 201 MHz RF cavities. The two superconducting focus-coil modules provide strong focusing at the absorber, ensuring that the transverse betatron function is minimised at this position and enhancing the cooling effect. All beam particles are detected individually by two identical Scintillating fiber trackers in 4T solenoids, situated upstream  
50 and downstream of the cooling section. The beam emittance is reconstructed, by measuring the spatial coordinates and momentum ( $x, y, p_x, p_y, p_z$ ) of each muon.

The particle content of the beam is measured by a dedicated system of detectors situated upstream and downstream of the cooling section and designed to provide precise muon, pion and electron identification. The upstream part includes two Time-of-flight hodoscopes (TOF0 and TOF1)  
55 and a Cherenkov detectors (CKOV). The downstream part combines another Time-of-flight hodoscope (TOF2) and a calorimeter system. The calorimeter system consists of the KLOE-Light (KL) lead-scintillator sampling calorimeter, similar to the KLOE design [30], but with thinner lead foils, serving as a preshower for the totally-active Electron-Muon ranger (EMR), situated behind him.

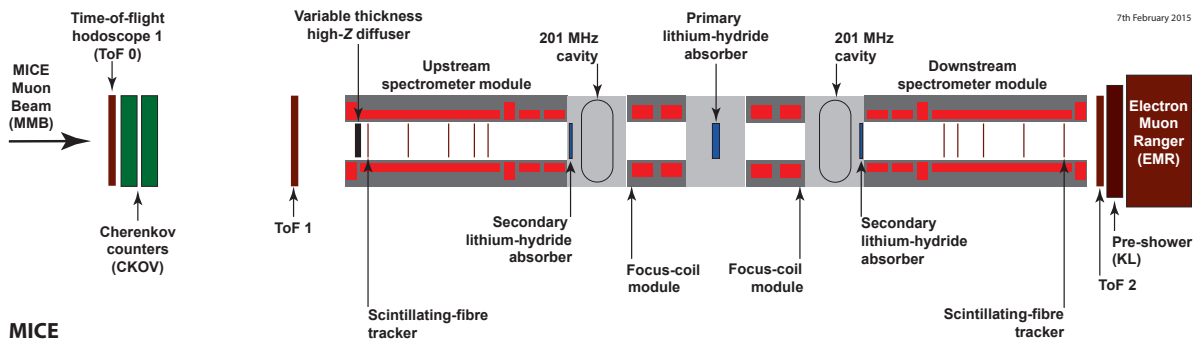


Figure 2: Schematic view of the MICE experiment.

MICE will measure the normalised transverse emittance  $\epsilon_N$  with a precision of  $\sigma_{\epsilon_N}/\epsilon_N \sim 0.1\%$   
60 when 6% cooling effect is expected for a muon beam with a nominal momentum of  $200 \text{ MeV}/c$  and 4D normalised emittance  $\epsilon_N = 5.8 \pi \text{ mm rad}$ .

### 1.3 Electron-Muon Ranger (EMR)

EMR is a fully active scintillator detector. It can be classified as tracking calorimeter, since its granularity allows for track reconstruction. The primary purpose of the detector is to distinguish muons from their decay products, rejecting events in which the muon decays in-flight along the cooling section [6]. This allows for the selection of a muon beam with a contamination below 1%. The range of the muon track can be measured, providing an estimate of the momentum of the muon.

The construction of the detector started in the early 2011 and in October 2013 the detector was fully commissioned with beam during one month of a dedicated data-taking at RAL. In 2014 the detector was upgraded, including a replacement of the single-anode photo-multiplier tubes and installation of a new high-voltage system.

## 2 Design

The EMR is built of triangular scintillator bars arranged in planes. One plane contains 59 bars and covers an area of  $1.27 \text{ m}^2$ . Each even bar is rotated by 180 degrees with respect to the odd one. A cross-section of bars and their arrangement in a plane is shown in Figure 3. With this configuration there is no dead area for particles crossing a plane with angles less than 45 degrees from the beam axis.

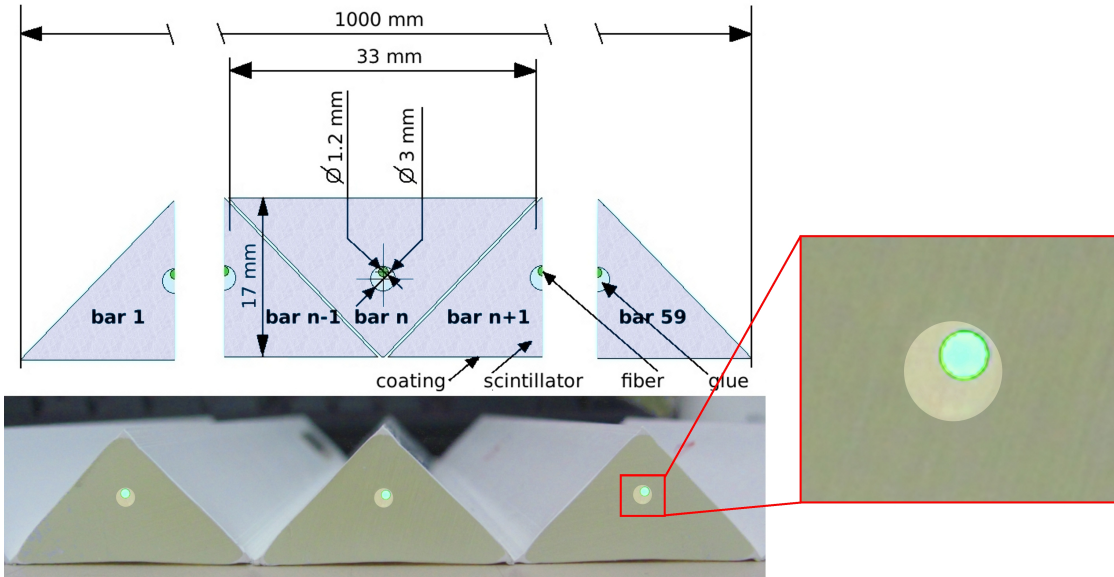


Figure 3: EMR bar cross-section and bars arrangement in a plane. There are 59 bars per plane.

The light, produced when a particle crosses a bar, is collected by a wave-length shifting (WLS) fiber glued inside the bar. At both ends of a bar the WLS fiber is coupled to a clear fiber that transfers the light to a photo-multiplier (PMT). The clear fibers are protected with rubber sleeves and packed in aluminum fiber boxes as drawn in Figure 4. In order to reduce the bending radius, which affects light attenuation, each fiber has an individual length. The two bunches of clear fibers coming from the two sides of a plane are glued into different types of connectors. One is designed to match a multi-anode PMT, when the other one matches a single-anode PMT.

Two planes attached to each other via aluminum profiles form a rigid structure called module (Figure 5). The full detector contains 24 modules as shown in Figure 6. Panels cover all sides of the detector in order to insure a light-tightness. The signal coming from each multi-anode PMT is

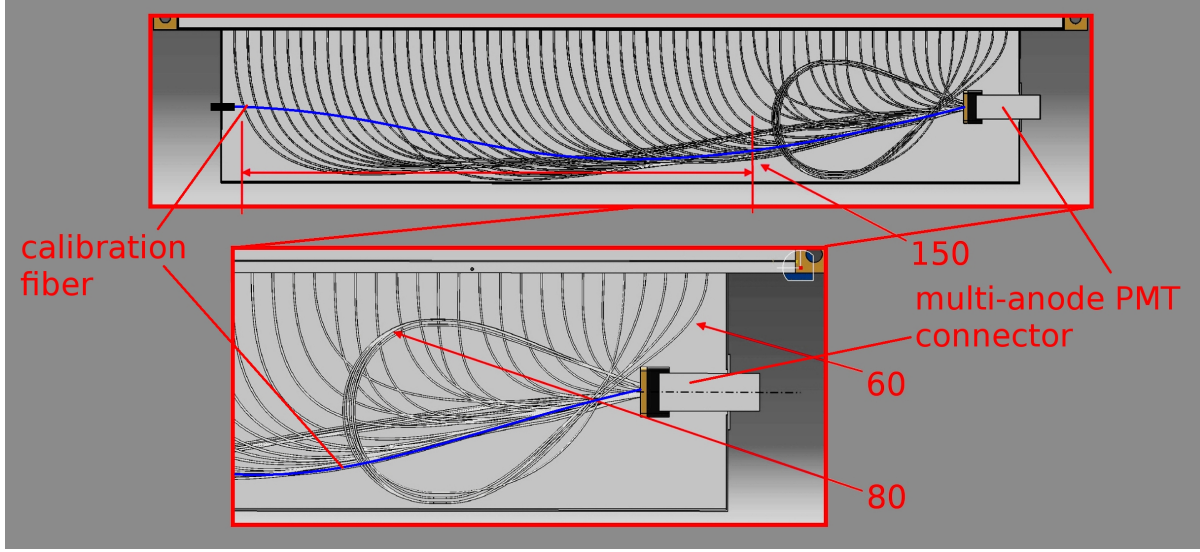


Figure 4: A package of clear fibers in a fiber box. Multi-anode PMT connector is shown. The fiber box for a single-anode PMT connector has similar structure. The last 5 fibers are looped in order to have largest possible bending radius. The bending radius of some of the fibers is indicate in red. The calibration fiber is also shown.

read-out and processed by a front-end board attached directly to the fiber box as shown in Figure 5. The single anode PMTs is equipped whit a voltage divider and the analog signal is sent outside the detector for digitization.

A calibration system was installed inside the enclosure of the detector in order to monitor the drift of the gain and the quantum efficiency of the PMTs. This system is made of a LED driver distributing light homogeneously to 100 fiber. Each fiber box is connected to one of the calibration fibers through a dedicated connector. Inside a fiber box a clear fiber connects the calibration fiber to the PMT (see Figure 4).

All cables inside the detector are feed through four patch-panels. There are 96 high-voltage, 6 low voltage, 48 analog, 48 digital, and one configuration cables in total. A support frame is designed to withhold the full weight of the sensitive volume with electronics ( $\sim 1$  tonne). In order to protect the front-end electronics from the magnetic field of the spectrometer solenoid, situated nearby the detector, a shielding plate is mounted on the side of the detector that faces the beam. The total weight of the detector is almost 2.5 tonnes.

## 2.1 Optical Elements

The scintillator bars were manufactured at an extrusion facility at Fermilab [7]. This facility also produced scintillators of different shapes for other experiments like: DO preshower detector, MINOS [8], Minerva [9], SciBar (K2K/SciBoone), Star, Mayn Pyramid Mapping, Hall-B JLAB, T2K-ND280, Double-Chooz, Amiga - Pierre Auger. Each bar is 110 cm long, 1.7 cm high and 3.3 cm wide with 3 mm hole along the bar for a wavelength shifting fiber. The scintillator is made of polystyrene pellets<sup>1</sup> as base, 1% PPO<sup>2</sup> as primary and 0.03% POPOP<sup>3</sup> as secondary fluor. Each bar is coated with TiO<sub>2</sub> reflector in order to increase light collected by the WLS fiber. Light output of the

<sup>1</sup>Dow Styron 663 W

<sup>2</sup>scintillator, 2,5-diphenyloxazole, C<sub>15</sub>H<sub>11</sub>NO

<sup>3</sup>wavelength shifter, 1,4-di-(5-phenyl-2-oxazoly)-benzene, C<sub>24</sub>H<sub>16</sub>N<sub>2</sub>O, spectrum peaks at 410 nm (violet)

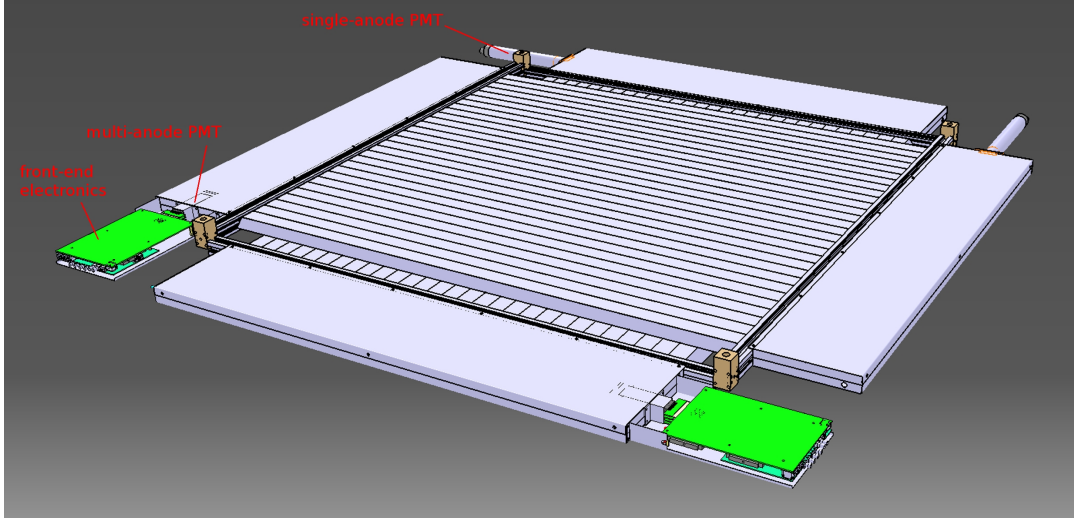


Figure 5: CAD drawing of one EMR module made of X and Y planes. There are two front-end boards per module.

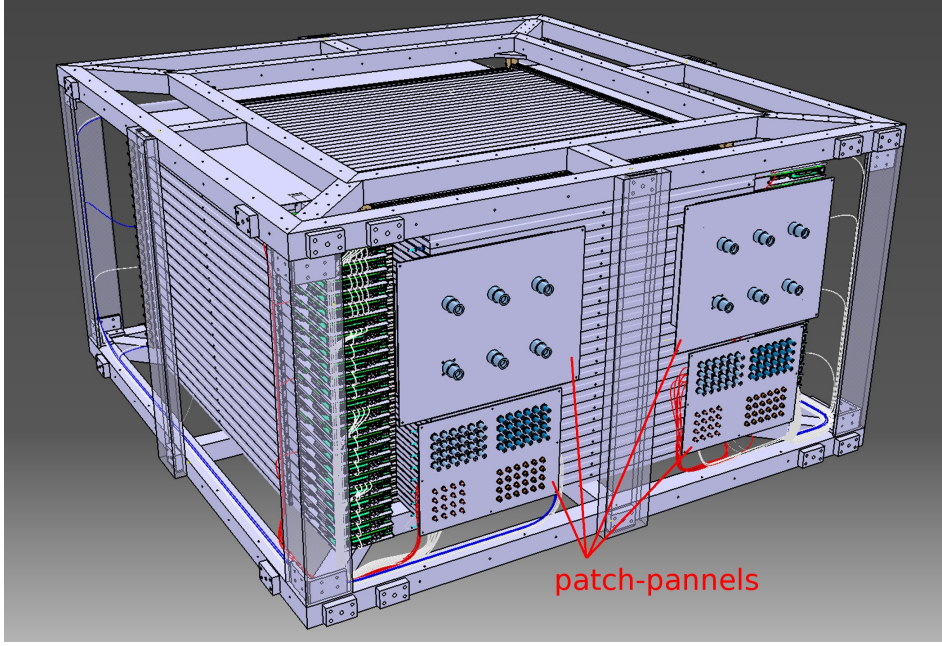


Figure 6: CAD drawing of the complete EMR detector. The external protective panels are not shown.

110 scintillator was measured [7] with a photo-multiplier (25% quantum efficiency) and it is around 17 photo-electrons.

The WLS fiber glued inside the bar is a double cladding 1.2 mm in diameter fiber, produced by Saint-Gobain Crystals [10]. The core material of the fiber is polystyrene with acrylic cladding. It has very large numerical aperture of 0.58 compared to 0.2-0.3 of graded-index multi-mode fiber used in data communications. Trapping efficiency is 3.5%. The light is absorbed in the blue part of the visible spectrum and re-emitted in green.

115 The clear fiber, used to transfer light from the ends of scintillator bar to the PMTs, is a 1.5mm

multi-cladding fiber produced by Kuraray [11] with special structure (S-type) that allows for better rigidity against bending. The aperture of this fiber matches to the one of WLS fiber so that insertion loss is minimal.

A special connector was designed to couple the clear fiber to the WLS fiber (see Figure 7). It has a small cylindrical enlargement which is meant to be filled with glue to fix the fiber in the connector. This configuration helps to avoid crimping the fiber since a sharp edge of the connector would easily damage it. As shown in Figure 7 the retaining clip (B) is screwed into the wavelength shifting fiber connector (A) so that clear fiber connector can be easily and safely attached. All these pieces are non-standard and could not be found on a market, therefore a special mold was designed to produce them using injection molding technique.

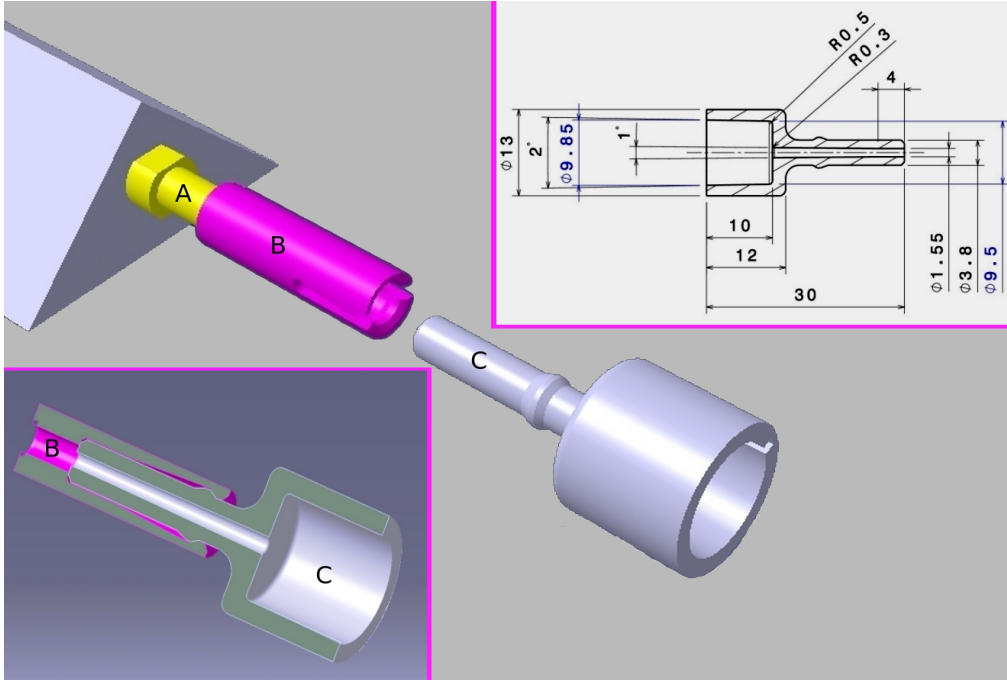


Figure 7: clear fiber connector (C) is attached to the wavelength shifting fiber connector (A) via retaining clip (B).

## 2.2 Photo-detectors

As it was briefly mentioned earlier the EMR has a dual readout. Each scintillator plane is equipped with a multi-anode PMT, which collects the light from the individual bars and a single-anode PMT which detects the integrated response of all bars in the plane.

The multi-anode photo-multiplier tube (MAPMT) is a 64-channel PMT produced by Hamamatsu (model R5900-00-M64 [12], see Figure 9, left). The spectral sensitivity matches to the emission spectrum of the wavelength shifting fiber. It is placed in a  $\mu$ -metal tube which serves as an additional shielding against the static magnetic field. Inside the  $\mu$ -metal tube, the PMT is aligned with respect to the fiber connector in such a way that each fiber shines only one channel. Therefore it was important to measure all dimensions of the PMT and especially position of the anode matrix with respect to the PMT case (Figure 9, centre). Figure 10 shows distributions of the measured dimensions (width and height) and displacements of the anode matrix for 53 MAPMTs. It was found that on average the matrix is shifted by 0.5 mm upwards (see Figure 9, right and Figure 10, bottom right). This

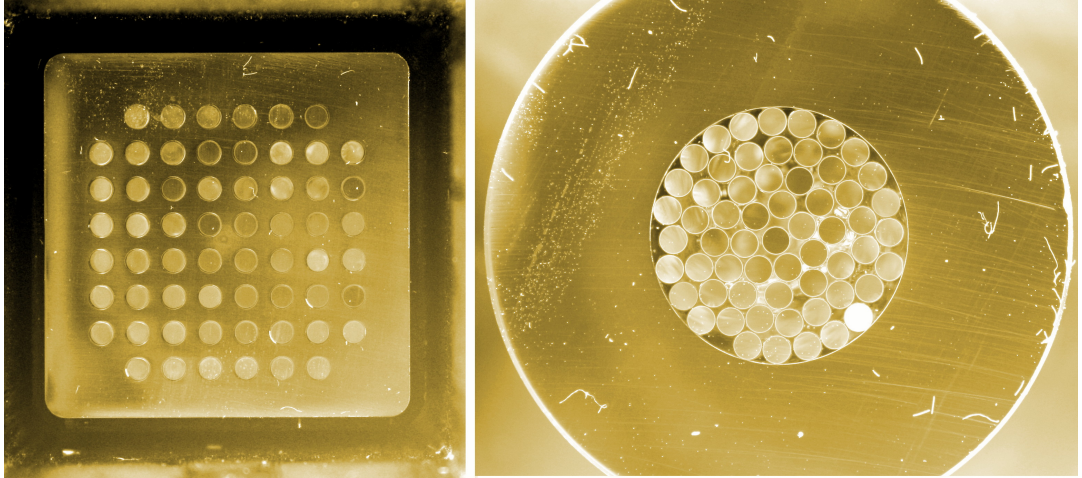


Figure 8: **Left:** multi-anode PMT connector. **Right:** single-anode PMT connector.

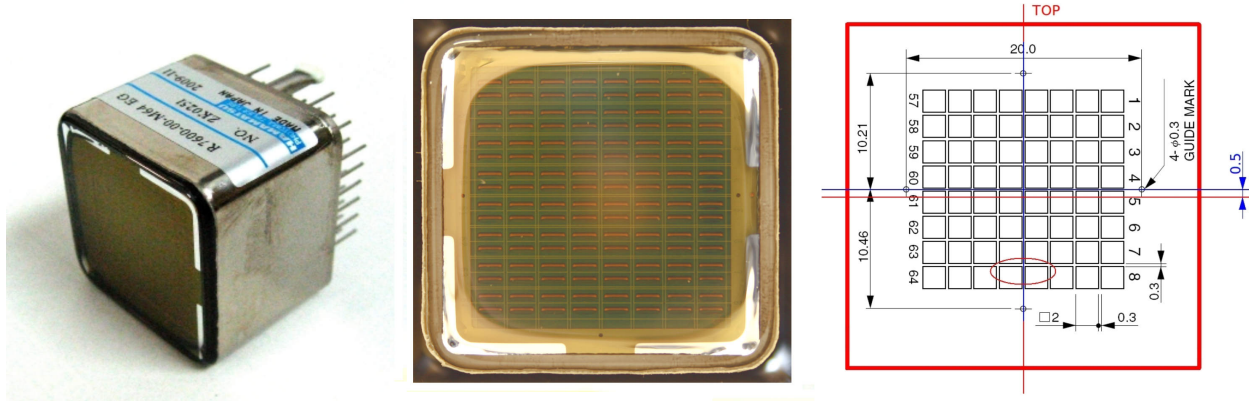


Figure 9: Multi-Anode PMT. **Left:** photo. **Center:** anode matrix. **Right:** anode matrix dimensions.

was taken into account in the design of the MAPMT fiber connectors.

As for the MAPMTs, the single-anode photo-multiplier tube (SAPMT) is placed in a  $\mu$ -metal tube. The EMR detector was initially assembled by reusing old SAPMTs, available after the disassembly of the HARP experiment [13]. These were 10 stage linear focused PMTs produced by Philips  
145 (model XP2972). A special selection procedure was developed in order to select the best samples for the assembly of the detector [14]. In 2014, during the upgrade of the detector, all Philips SAPMT were replaced by new SAPMTs produced by Hamamatsu (model R6427 [12]).

### 2.3 Electronics Layout

In MICE the spill is defined as the period when the target crosses the ISIS proton beam. The maximum spill repeating rate allowed by the MICE target system is  $\sim 0.75$  Hz. The overall principle of the MICE Data Acquisition (DAQ) system is that data is recorded only during the spill. The typical duration of the acquisition window (called also Spill gate) is between 1 and 3 ms. The accumulated digital data is kept in local memory buffers until the end of the spill, when the readout is performed.  
150

A schematic layout of the EMR electronics is shown in Figure 11. The multi-anode PMT is

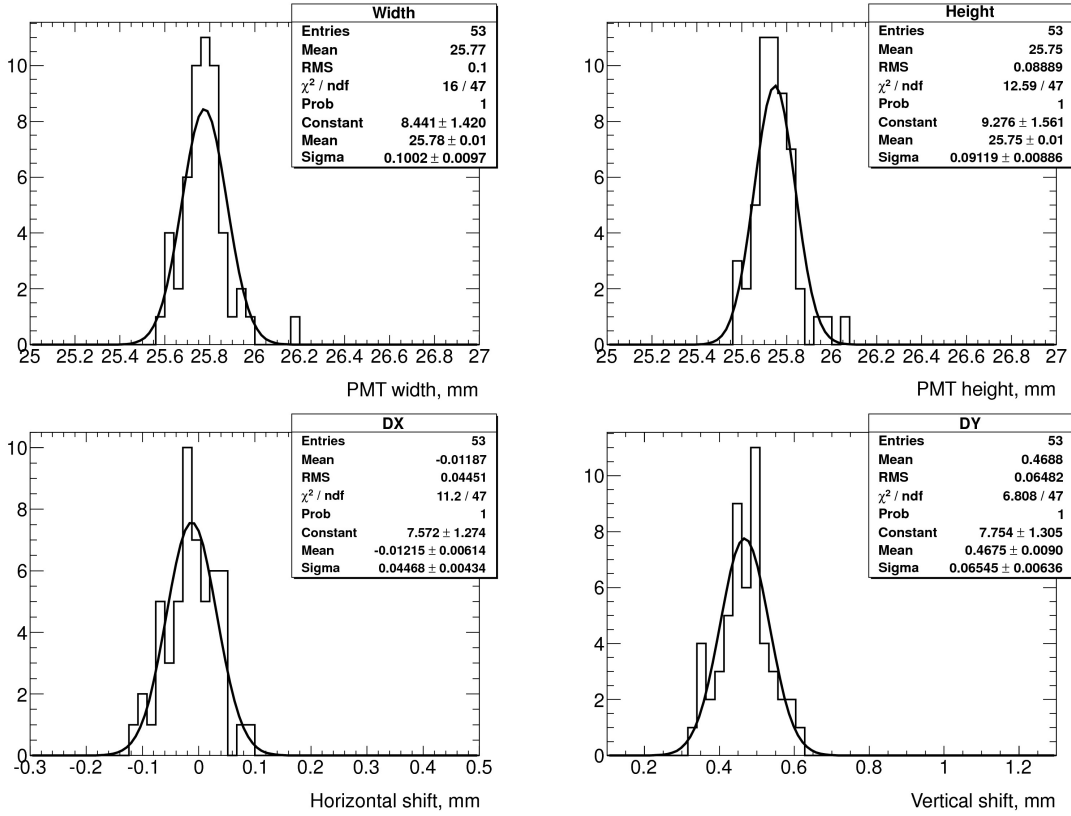


Figure 10: Distribution of Multi-Anode PMT dimensions.

connected via a flex cable to a front-end board (FEB), which processes the signal and sends it to a piggy-back digitizer-buffer board (DBB) for digitization and storage. The FEB is configured by the VME configuration board (VCB), which resides in the VME crate in the control rack. This board is able to configure up to 16 FEBs, therefore three of them are required for the full detector. The DBBs are readout by groups of six. In each group the first DBB is a master and the other five are slaves. All six boards are daisy-chained via ethernet cable and the master is connected to a VME readout board (VRB), which transfers all the data from the six DBBs to the DAQ computer. In the whole detector there are 8 groups of DBBs, i.e. 8 VRBs are installed in the control rack.

### 2.3.1 Front-End and Digitizer-Buffer Boards

The multi-anode PMT is readout by a dedicated front-end board equipped with piggy-back digitizer-buffer board [15], which stores hit information during a spill. Figure 12 show the full assembly that is mounted on every plane of the detector. It consists of a PMT attached to a voltage divider, which is connected to a FEB through a flex cable. This cable also creates additional pressure between the PMT and the fiber connector. The FEB is able to process all  $64^4$  signals of the MAPMT thanks to a 64-channel ASIC<sup>5</sup> called MAROC<sup>6</sup>[16].

The 64 analog signals are feed into the chip where they are processed in parallel: each channel consists of a pre-amplifier with a variable gain, a tunable slow shaper and a sample and hold circuit for the analog readout, a tunable fast shaper and a discriminator for the digital one. The MAROC

<sup>4</sup>Each EMR plane contains 59 scintillator bars which results in having 5 redundant channels.

<sup>5</sup>Application-Specific Integrated Circuit

<sup>6</sup>Multi Anode ReadOut Chip

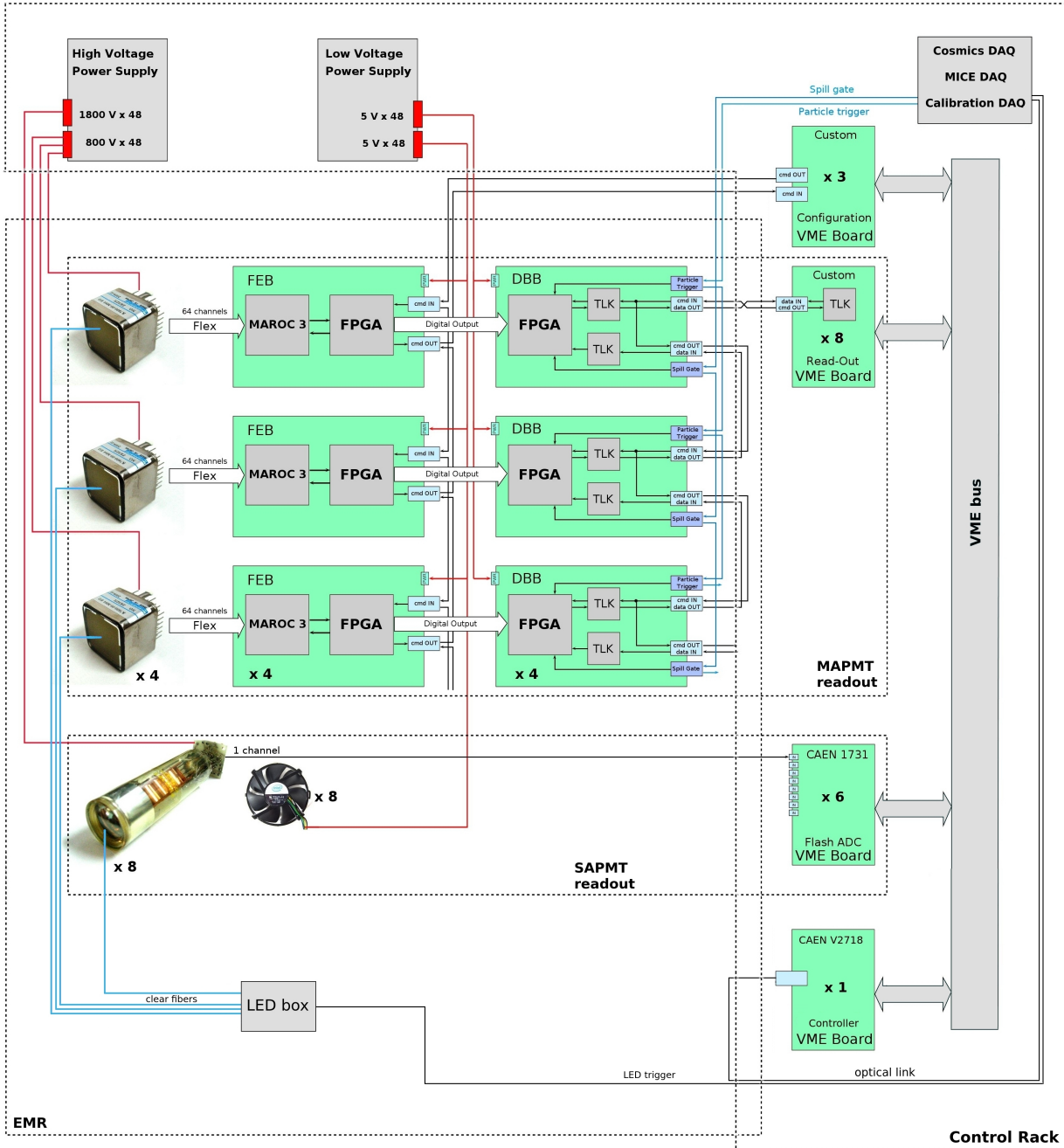


Figure 11: EMR electronics layout. **FEB:** front-end board for multi-anode PMT readout. **DBB:** digitizer-buffer board. **MAROC 3:** 64 channel readout ASIC for multi-anode PMT. **MAPMT:** multi-anode PMT. **SAPMT:** single-anode PMT.

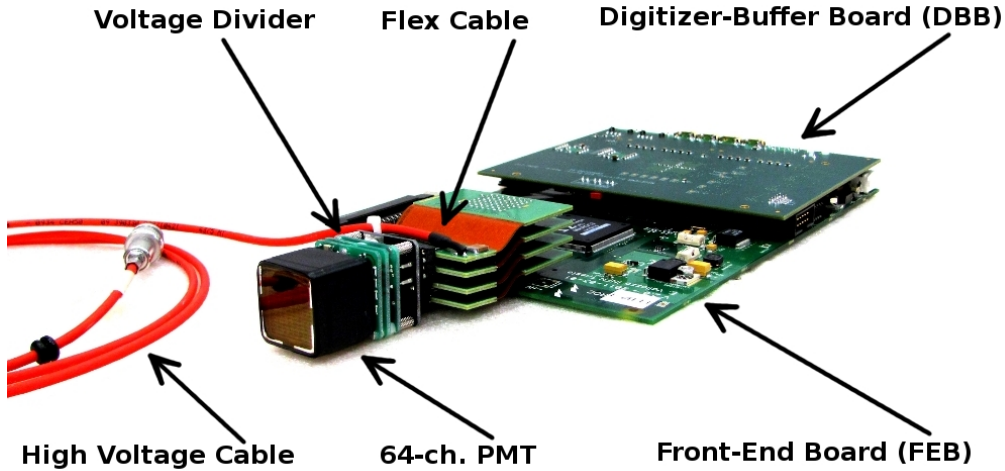


Figure 12: Front-end and Digitizer-Buffer board assembly.

ASIC provides 64 parallel digital outputs, which are forwarded to two high density connectors  
 175 where a DBB is plugged. The width of the discriminated signal represents a time over threshold measurement. One multiplexed analog output is also provided and this output is digitized by an external ADC (AD9220, Analog Devices). It takes tens of microseconds (depending on the MAROC configuration used) to process all the multiplexed signals and this dead time is not acceptable for the MICE DAQ duty cycle (a few hundred triggers per 1 ms spill). Therefore only time-over-threshold measurement is used since it is practically dead-timeless.  
 180

The function of the FPGA chip<sup>7</sup> is mainly to forward data from the MAROC to the DBB and to send configuration signals from the VCB to the MAROC and verify their status. The board has a separate power for analog and por the digital parts (both 5 V). The total power consumption of the board is 0.6 Amp.

185 The two essential roles of the DBB are to sample 63 of the channels coming from the FEB plus an external trigger signal and to store the accumulated digital data during the spill. It also has to transmit this data upon request of the acquisition system. The digitization starts when the board receives the so called Spill Gate signal from an external LEMO connector. The number of clock ticks from the beginning of the spill to the leading edge and trailing edge of every discriminated signal  
 190 coming from the FEB is recorded. The difference between the two measurements represents the time over threshold of the original signal. The clock sampling rate is 400 MHz (2.5 ns resolution). The external trigger signal is feed into one of the 64 input channel and is treated as any other signal. This signal does not serve as a trigger for the DBB itself, since the board records continuously and all signals arriving within the spill gate are digitized and recorded. Nevertheless, the timing of the  
 195 trigger signal is important, because it is used to identify the records belonging to a given particle and for matching with the measurements recorded by the other detectors. The board also calculates the width of every spill, counts the number of spills, number of triggers in the spills, and number of hits in every channel.

The architecture of the DBB is organized around a single FPGA<sup>8</sup> that performs the sampling,  
 200 data buffering, and data-flow control functions of the board. Internal memory of the FPGA, configured as FIFO, is used to store the event data which is a collection of leading and trailing edge

---

<sup>7</sup>Altera Cyclone II (EP2C35F484C8N)

<sup>8</sup>Altera Stratix II (EP2S30F484C3N)

timestamps that occurred on each channel during a specific spill. Two gigabit transceivers<sup>9</sup> are interfaced to the FPGA to provide the physical transmission channels and form an upstream command link and a downstream data link. Six DBB's are grouped together and daisy-chained with upstream and downstream links via ethernet cable. The first DBB in each group is directly connected to the VRB via four coaxial cables.

### 2.3.2 VME Configuration Board

The VCB is a single FPGA<sup>10</sup> board designed to perform configuration of the MAROC chip on the FEB. The communication between the two boards is realized via LVDS<sup>11</sup> signals driven and received by LVDS drivers/receivers directly connected to a corresponding FPGAs. The MAROC chip is configured by TTL<sup>12</sup> signal composed of 830 bits which code the configuration parameters. The VCB can readout from the FEB the digitized measurement of the MAROC analog output, but this is not implemented in the current design. The board communicates with the DAQ computer through the VME bus via the VME controller.

### 2.3.3 VME Read-Out Board

One VRB performs the readout of a group of six DBBs. It is a single FPGA<sup>13</sup> board with a gigabit transceiver<sup>14</sup>, which drives the communication with the DBBs and four high-speed 16M-bit static RAMs<sup>15</sup>, providing a local memory buffer. During the readout cycle, the transfer of the data between the DBBs and the DAQ computer is executed in two steps. First, after a request from the DAQ computer, the VRB starts transferring data from the 6 DBBs. The gigabit transceiver is used for this and the received data is temporarily stored locally. The four static RAMs, each organized as 16 bits data words, are grouped in two pairs, providing the record of the DBB data, which is originally structured in 32 bits data words. Once the first part of the transfer is completed, and all the data accumulated by the 6 DBBs during the spill is available in the local memory buffer of the VRB, the DAQ computer sends a second request which triggers the transfer of this data over the VME bus.

Additional LVDS input/output connector is available at the front panel of the board. This connector does not have a specific function, and was used mostly for debugging.

### 2.3.4 Fast ADC Board

A waveform digitizer V1731, made by CAEN [17] is used to readout signals from single-anode PMTs. The digitizer has a sampling frequency of 500 M samples per second (2 ns timing resolution). A pulse shape of each input signal is digitized by 8 bit ADC and continuously written in a circular memory buffer. When a trigger<sup>16</sup> arrives the FPGA writes a certain number samples into the buffer, which then is available for readout via the VME bus.

## 2.4 Mechanics

Total weight of the sensitive volume of the detector is almost 1 tonne. During construction and installation it is required to rotate and move the detector; besides that it is meant to be transported

---

<sup>9</sup>TLK1501

<sup>10</sup>Altera Cyclone II (EP2C50F484C8N)

<sup>11</sup>Low-Voltage Differential Signaling, communication protocol.

<sup>12</sup>Transistor-Transistor Logic

<sup>13</sup>Altera Cyclone II (EP2C50F484C8N)

<sup>14</sup>TLK1501

<sup>15</sup>IS61WV102416BLL-10TLI - SRAM, 16Mbit, 10ns, 48TSOP

<sup>16</sup>The same trigger signal, received by the DBBs

in a truck over more than 1000 kilometres. Therefore a reinforced support frame (see Figure 13) was designed so that it can withhold the weight of the sensitive detector and all the stress that may happen during the transportation and installation. In its final position the EMR is installed in such a way so that planes are located vertically perpendicular to a beam direction.

240

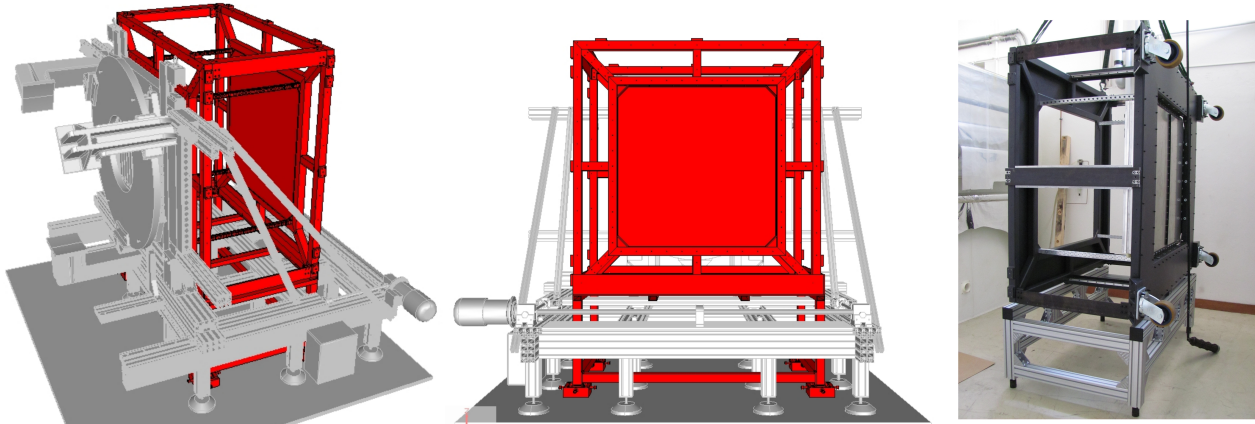


Figure 13: EMR support frame. When installed in the MICE experimental hall, the EMR is integrated into the support structure of the other downstream particle identification detectors.

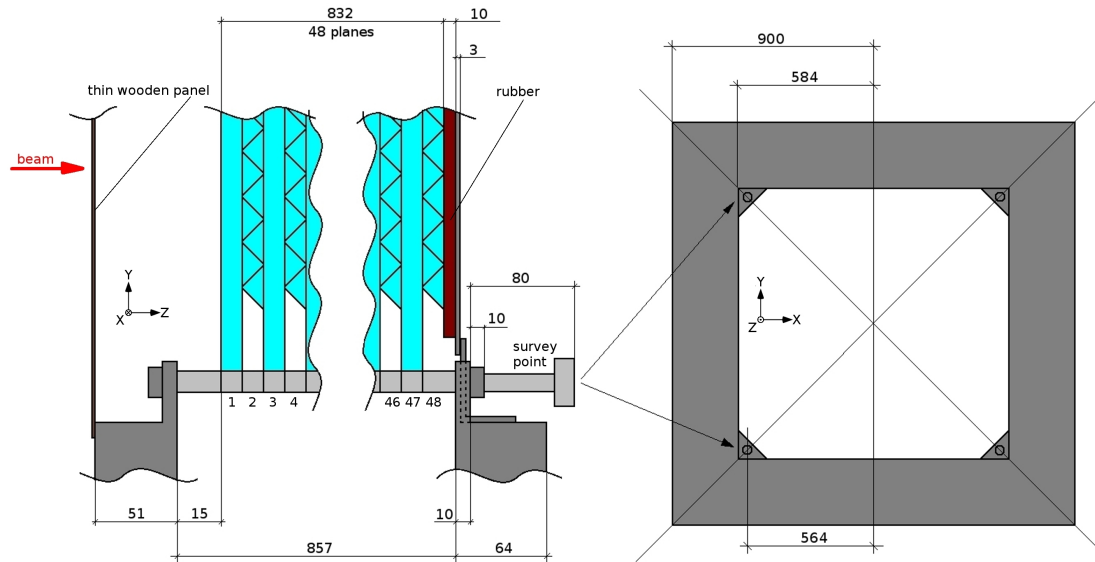


Figure 14: EMR dimensions (mm).

Figure 14 shows the location of the sensitive volume with respect to the support frame. The frame is covered with panels so that the whole volume is light-tight. 5 cm thick iron plates are used to form a front panel magnetic shield (total weight 755 kg). The opening in the shielding panel, which matches the size of the sensitive volume, is closed with a thin wooden end cap. The back panel is closed with a metal end cap (since it holds the weight of the detector during assembly, when it is in horizontal position).

245

### 3 Construction

All the construction work of the detector was done at University of Geneva. It is well known that exposure to ultra-violet (UV) light or high temperature can damage the polystyrene molecules. This  
250 is especially important for fibers, because the damage decreases the light transmission. Therefore all activities related to fibers and scintillators were performed in a UV clean room, i.e. lights and windows were covered with UV-protective films, with air conditioning that kept the temperature around 25 °C.

As it was already mentioned, the scintillator bars were produced at Fermilab. The first step  
255 in the construction was to glue the wavelength shifting fibers into the bars. Transparent epoxy<sup>17</sup> was used to glue the WLS fiber in order to increase the light collection efficiency. Although 2832 bars were required for building the full detector, 3150 bars were glued and assembled with fiber connectors in order to provide enough spares available. In the second step, both faces of the bar's  
260 fiber connectors were polished with a special polishing machine. Four different grades of sand paper are used to achieve a mirror like quality of the polished surfaces. The last step is performed using a 1μm grade diamond-based polishing paper.

Fiber bundles made of 60 clear fibers (see Figure 15) were manufactured. In the bundle, each fiber has an individual length, providing a minimum bending radius, when connected. A fiber connector (see Figure 7, bottom right) is glued at one end of each fiber. At the other end all fibers are glued  
265 either in multi-anode or single-anode PMT connector (see Figure 8). Once glued, both fiber and PMT connectors are polished on a bench, similar to the one used to polish all bar connectors. In total there were 96 fiber bundles (48 for each type of PMTs).



Figure 15: Clear fiber bundles. **Left:** fiber pre-cut to the specified length. **Centre:** PMT connector. **Right:** fiber connector.

#### 3.1 Quality Tests

Numerous quality test were implemented, in order to assure the best possible performance of the  
270 different components of the detector.

A dedicated bar quality test bench was constructed in order to test the light transmission of each bar, including the transmission of the WLS fiber and the quality of the two connectors. The test bench consisted of a LED<sup>18</sup> system, a holder for 4 scintillator bars and a digital camera, all placed in a light-tight box. The LED system included blue LED, light mixing box and diffusers,  
275 providing that the light is homogeneous at the outputs, where the bars under test are connected. The camera was taking a photo of the four connectors at the opposite side of the bars. Out of four bars one was a reference and the measurements were normalized to it in order to take into account

<sup>17</sup>Prochima E30 water effect resin ????

<sup>18</sup>Light Emitting Diode

the effect of a possible LED instability and to have a possibility to compare different measurements. An automated program was used to analyze the photos (Figure 16 - left) and to calculate the light intensity of each bar. Figure 16 - right shows the distribution of the measured relative residuals of the light intensity. The relative residual was defined as the difference between the measured value and the average value divided by the average. Only bars with a relative residual intensity above -0.15 were accepted for plane assembly. Out of 3150 tested bars 305 bars (9.7%) did not pass that requirement and were rejected.

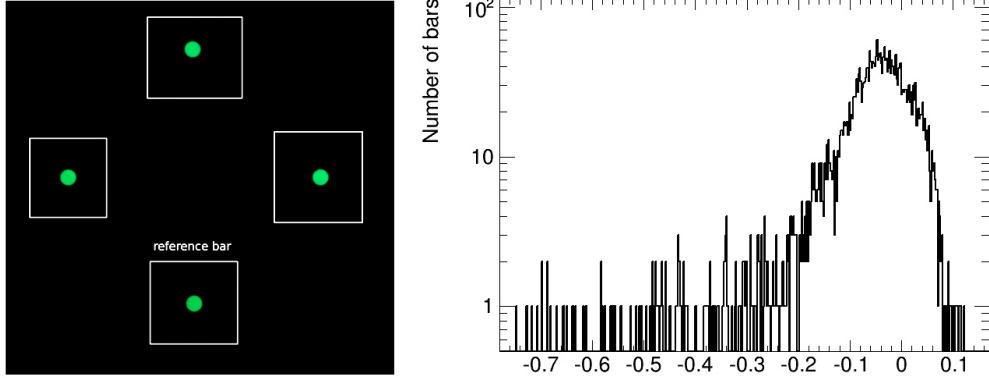


Figure 16: Bar quality test measurements. **Top left:** an example of one measurement, bottom bar is a reference. **Top right:** distribution of the relative residual intensity.

A similar test was used to examine each EMR plane after the assembly [18]. An LED tube attached to a single-anode PMT connector was used to send light through the fibers (WLS and clear) all the way up to the multi-anode PMT connector, where a picture of the PMT mask was taken by a camera. Again, an automated program was used to analyse the photos (Figure 17 - left) and to calculate the relative residuals of the light intensity of the individual channels (Figure 17 - right). This test verified the light transmission of the fiber bundles, but also the quality of the interconnections between the WLS fibers and clear fibers. A plane was accepted only if the relative residual intensity of all 60 channels were above -0.4.

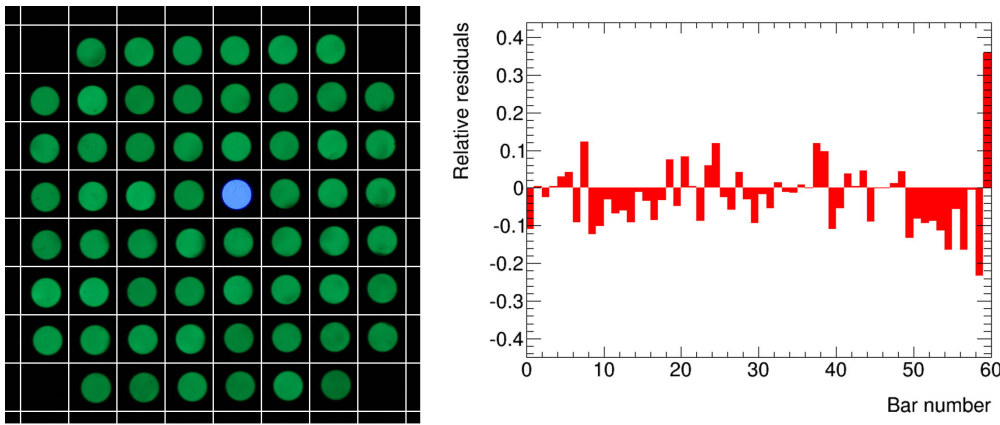


Figure 17: Example of plane quality test for one plane. **Left:** PMT mask. **Right:** relative residual intensity values for 60 channels, the last value is for a calibration channel.

A separate test bench was setup in order to verify the functionality of the three major components of the EMR electronics: the multi-anode PMTs, the front-end boards and the digitizer-buffer boards.

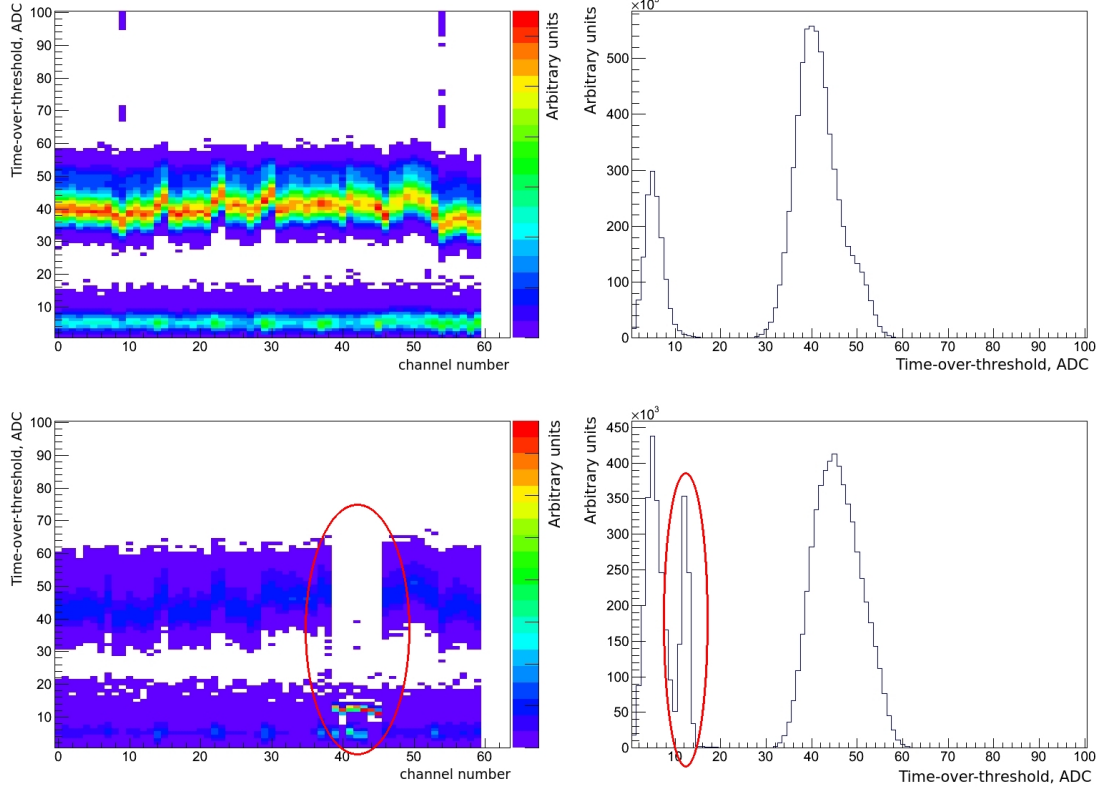


Figure 18: Electronics quality tests. **Top:** functional board. **Bottom:** faulty board. **Left:** Time-over-threshold (ToT) as a function of the channel number. Typical response to LED signal is around 40 ADC. Pedestal signal is around 5 ADC. Any faulty channel does not produce an adequate signal as seen in the bottom plot (channels 38 to 45). **Right:** Distribution of the time-over-threshold (ToT) for all channel in a given board.

295 It reproduced the full electronics chain used to readout the detector with the only difference that the  
 light is generated by a LED, power by a variable amplitude pulser. The LED was attached to the  
 MAPMT injecting light in all channels at the same time. The final measurement that is provided  
 by the system is a time-over-threshold (ToT) of the PMT signal. During the tests this measurement  
 is used as a figure of merit to characterize the electronics chain (PMT, FEB and DBB). Figure 18  
 300 shows an example of a fully functional electronics chain (top) and an example of a faulty electronics  
 (bottom). Only boards, exhibiting a behaviour as in Figure 18 - top, were accepted for installation  
 in the detector.

### 3.2 Examining the performance with the LED calibration system

After the assembly was completed, the detector was fully powered and tested during a few days  
 305 of LED and cosmics data collection. As described above, the detector is equipped with a build-in  
 LED system for calibration. Light is transported from a LED driver through 96 clear fibres to each  
 SAPMT and to one specific channel of each MAPMT (test channel). The LED driver was tuned  
 with a variety of voltages ranging from 11.0 V to 22.0 V by steps of 0.5V. For each setting, 10000  
 310 pulses were recorded. The mean ToT in the test channel of a MAPMT is represented as a function  
 of the LED driver voltage in Figure 19. The green area represents the voltage region for which the  
 recorded ToT is consistent with the signature of a minimum ionizing particle.

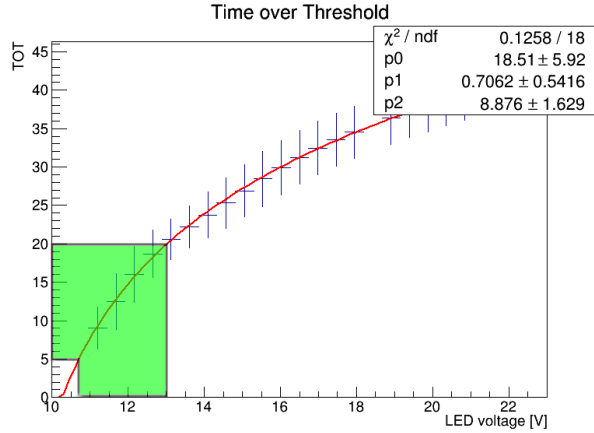


Figure 19: Mean ToT in the test channel as a function of the LED driver voltage.

The collected data was used to investigate the dependence between the ToT measurement and the original total charge of the MAPMT signal. This can be done, assuming that the total charge of the signal in the test channel of the MAPMT is proportional to the total charge  $Q$ , recorded by the SAPMT when both receive light from the same LED pulse. An exponential behaviour of the form

$$Q = e^{(a \times \text{ToT} + b)} \quad (1)$$

is expected, with  $a$  and  $b$  being two unknown parameters. The parameter  $a$  gives the slope of the exponential in log scale and depends on the EMR characteristics such as the scintillation time constant, the FEB shaping function or the threshold level. As a result, we expect this parameter to be constant for each plane with small variations. The parameter  $b$ , on the other hand, depends on the two PMTs gain and can vary significantly from one plane to another. These two parameters were obtained experimentally by fitting the relation  $Q$  vs. ToT for each individual plane of the detector.

### 3.3 Examining the performance with cosmic rays

Cosmic rays present an ideal source of particles that can be used to characterize, debug and tune the detector. Cosmic rays that reach the detector are typically multi-GeV muons that traverse the EMR without stopping. An externally generated 3 ms signal was used in order to reproduce the timing structure of the so called Spill gate signal, used by the MICE DAQ system. A coincidence between the SAPMT signals from two planes and the Spill gate signal was used as a trigger.

The EMR planes were perpendicular to the ground at the time of this test. Data was taken for 60 hours and yielded  $\sim 2.23 \times 10^5$  triggers. The raw measurements of the EMR comprise the hit time and ToT for each bar and the integrated plane charge. The two planes used as trigger did not record a plane charge. The amount of hits recorded in each bar was of order  $\sim 10^3$ . The test revealed only 5 dead channels ( $\sim 0.2\%$  of the detector). A typical cosmic event is shown in Figure 20.

#### 3.3.1 Cosmic muon signature

Cosmic muons are minimum ionizing particles and hence deposit on average the same amount of energy in each plane. The muon typically hits two triangular bars in a plane, by design. The additional hits come either from crosstalk or noise (e.g. third hit in plane 26 in figure 20, top-left). All hits from muons have approximatively the same time offset with respect to the trigger. To

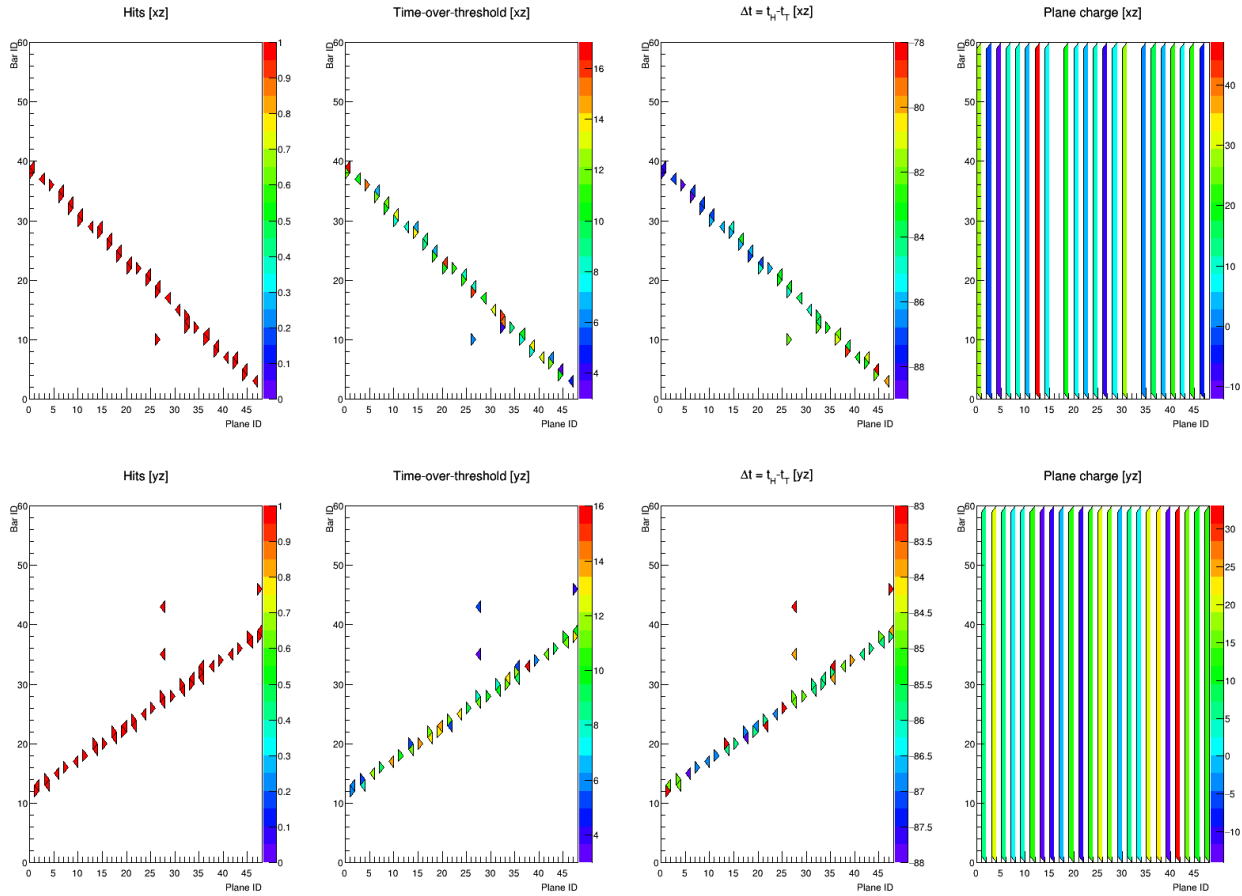


Figure 20: Cosmic muon event in the EMR in the  $xz$  (top) and  $yz$  (bottom) projections. From left to right: hits per bar, ToT, hit time with respect to the trigger and plane charge.

separate the true hits from the noise, a cut on the time difference between a bar hit and the trigger was applied. A thorough study of the crosstalk was conducted and is presented in section 3.4.

340 Figure 21 shows the time and ToT structure of the hits recorded in the MAPMT for the whole sample of cosmic data. The hits come prior to the trigger in the readout chain due to the delay in the logic box. Time walk affects the timing so that the lower amplitude signals come later on average. The distinctive spike present at  $\sim 15$  ADC counts in the ToT distribution is an artefact, originated from the nonlinear connection between the ToT measurement and the total charge of the  
345 original analog signal.

The SAPMTs were used to measure total charge in planes. The digitizers store waveforms of signals associated to triggers within a certain acquisition window. These waveforms are integrated in a signal window off-line taking into account the pedestal positions in order to compute the total plane charge, as shown for the whole cosmic data sample in Figure 22.

### 350 3.4 LED-based crosstalk analysis

The EMR is susceptible to two types of crosstalk: optical crosstalk, i.e. a single fibre of a bundle shining on more than one channel of the MAPMT mask, and anode crosstalk, i.e. a photo-electron leaking from a dynode to an adjacent accelerating structure. An analysis was developed in [19, 20] to evaluate the significance of this phenomenon.

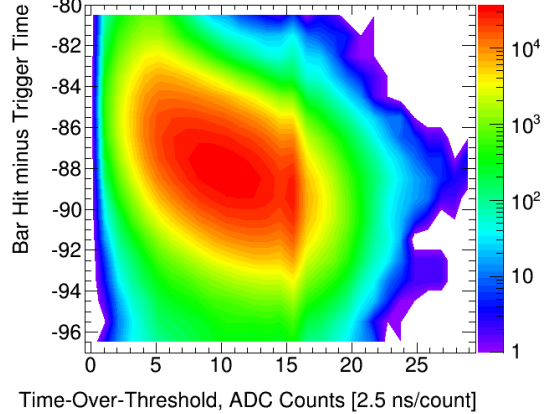


Figure 21: Energy and time structure of the hits recorded in the MAPMT for cosmic muons (MIP signals).

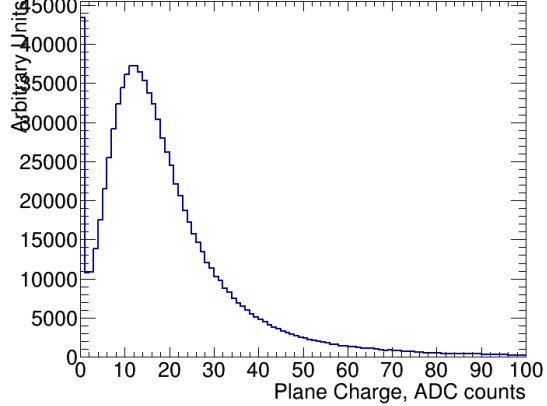


Figure 22: Distribution of the charge recorded in the SAPMT for cosmic muons (MIP signals).

355 Cosmic or beam data are poorly suited for this analysis. A real particle often hits two bars or more within the same plane which makes it impossible to disentangle real signals from crosstalk in neighbouring channels. An LED calibration system is a more reliable tool to drive the analysis. The test channel, connected to the LED light source, has four directly adjacent channels: top (N), bottom (S), left (W) and right(E). This method ensures that hits in the adjacent channels are caused  
360 by crosstalk only.

The first parameter that characterizes the crosstalk is the charge ratio,  $R_Q^i$ , between the signal amplitude in an adjacent channel  $i$  and the primary amplitude in the test channel. As explained already, the charge is not measured directly but is related to the ToT through Equation (1). The ratio subsequently reads

$$R_Q^i = \frac{Q_i}{Q_0} = \frac{\exp[aToT_i + b]}{\exp[aToT_0 + b]} = \exp[a(ToT_i - ToT_0)]. \quad (2)$$

365 The ratio is measured for the highest achievable LED voltage setting as the resolution evolves as  $1/\sqrt{Q}$ . The ratio measured in the 192 readout channels (directly adjacent N,S,W,E channels of each plane) is represented in Figure 23. The fraction of the original signal that typically leaks in adjacent channels is  $4.49 \pm 0.11\%$ .

370 The second parameter used to characterize the crosstalk is the rate. The measured quantity is the ratio  $R_N^i$  of hits in a surrounding channel  $i$  to the total amount of pulses generated in the test channel. This quantity is measured in the 192 readout channels for a voltage setting in the green area of Figure 19, corresponding to MIP-like signals, and represented in Figure 24. The average rate fraction is  $0.20 \pm 0.01\%$ , well within design requirements.

375 The measurement of the crosstalk rate in the adjacent channels also provides a measurement of misalignment of the MAPMT mask with respect to the fibre bundle. If a mask is shifted, light is more likely to leak and create signals in the channel towards which it is offset. The centre of the mask with respect to the centre of fibre bundle is computed through

$$(x_C, y_C) = \left( \frac{\sum_i x_i w_i}{\sum_i w_i}, \frac{\sum_i y_i w_i}{\sum_i w_i} \right), \quad (3)$$

with  $(x_i, y_i)$  the coordinates of the surrounding channels and  $w_i$  the amount of hits recorded in them. The resolution is function of  $1/\sqrt{N}$ ,  $N$  the amount of signals recorded, hence a high voltage

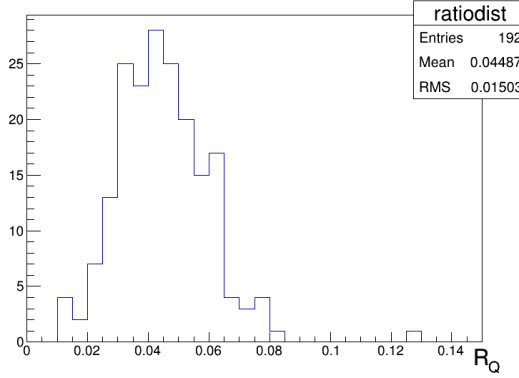


Figure 23: Fraction of the original charge that can leak in adjacent channels.

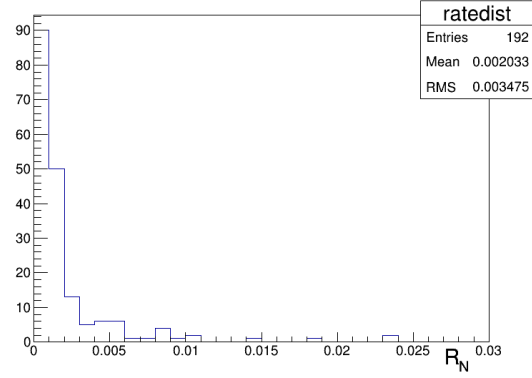


Figure 24: Fraction of the time a signal produces crosstalk for a typical MIP energy loss.

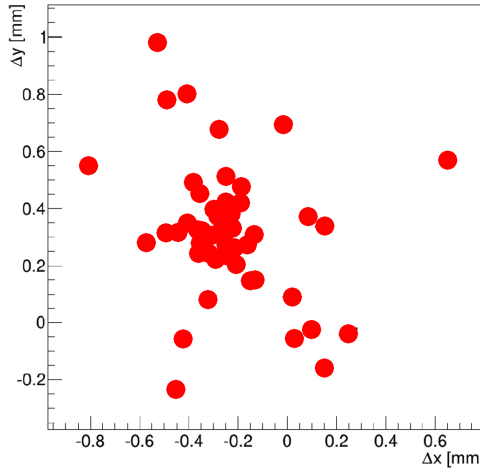


Figure 25: Misalignment of the MAPMT mask with respect to the fibre bundle for the 48 planes.

380 is chosen for this analysis. The results for the 48 planes are presented in Figure 25. There is a noticeable cluster around  $(-0.3, 0.3)$  but nothing that could impair the detector.

### 3.5 Cosmic-based channel mismatch analysis

The design of the EMR, involving the connection of external clear fibres to internal WLS fibres, leaves room for human error in matching the two correctly. A dedicated analysis was designed in order to verify the consistency of this connection across the 2832 bars in the detector. This analysis [19, 20] uses the distance between each bar hit and its particle track as a tool to estimate the likelihood of mismatch. A mismatched channel is not reconstructed in the right location and is, on average, significantly less consistent with the other measurements in a reconstructed particle track. Cosmic muons were particularly suited for this procedure as they traverse the whole detector in straight lines, without stopping and provide full coverage. When the data sample used in this analysis was recorded, the EMR was positioned up right with planes vertically oriented. Two cuts are applied to the data sample in order to rid the muon tracks of artificial hits caused by crosstalk and noise. Crosstalk signals were rejected by placing a lower limit on the ToT measurement. Restricting the delay between the trigger time and the hit time to a small interval was used to rid of most of the

395 noise. To reconstruct tracks and calculate the distance of each hit from its particle trail, the hits were  
 split into two projections  $qz$ ,  $q = x, y$ . The plane ID of the channel hit provided the  $z$  coordinate and the bar ID provided either  $x$  or  $y$  coordinates, depending on the plane orientation. The  $(q_i, z_i)$  coordinates were those of the barycentre of the triangular section or the bar corresponding to the hit.  
 400 For a linear fit  $q = a_q z + b_q$ , the absolute distance between a hit  $(q_i, z_i)$  and the track within a plane reads  $\Delta q_i = |q_i - (a_q z_i + b_q)|$ . For intuitiveness, distances are expressed in bar units (b.u.) in the following developments. A b.u. corresponds to the height of the triangular section or equivalently to the half width of its base.

The critical secondary variables, measured for each channel are the ratios of mismatch,  $R_i$ . Given an integer  $i$ , the ratio  $R_i$  corresponds to the fraction of the sample for which the bar is within  $i \pm 2/3$  b.u. off-track. For a distance distribution  $f(\Delta y)$ , the ratio is defined as  
 405

$$R_i = \frac{\int_{i-2/3}^{i+2/3} f(\Delta y) d(\Delta y)}{\int_0^{2/3} f(\Delta y) d\Delta y + \int_{i-2/3}^{i+2/3} f(\Delta y) d\Delta y}. \quad (4)$$

For instance, the ratio  $R_1$  represents the probability of a bar of being mismatched by exactly 1 b.u., i.e. to be swapped with an adjacent bar. It is shown in [20] that  $R_i$  is theoretically estimated to take values summarized in table 1 for different scenarios. The  $X - Y$  asymmetry of the ratio  $R_i$  is due to the different angular distribution of muons seen by the vertical and the horizontal bars.

	Matched		Mismatched	
	$xz$ proj.	$yz$ proj.	$xz$ proj.	$yz$ proj.
$R_1$	25.3 %	32.2 %	62.6 %	66.1 %
$R_{i \geq 2}$	$\sim 0\%$	$\sim 0\%$	$\sim 100\%$	$\sim 100\%$

Table 1: Mismatch ratios,  $R_i$ , for matched and mismatched bars in the two projections.

410 The mismatch ratio for adjacent bars was measured and is represented for each channel in fig. 26. The ratio distribution is represented next to it in log scale. The bulk of the distribution is centred around 28.88 %, consistent with the weighted average of the theoretical predictions for the two projections. Bars 47 and 48 of plane 44 record a ratio of  $62.5 \pm 3.5\%$  and  $57.2 \pm 3.2\%$ , respectively, significantly superior to the bulk and in agreement with the prediction. Their proximity 415 to each other corroborates the hypothesis of a channel swap. The mismatch is fixed at the level of the channel map in the reconstruction.

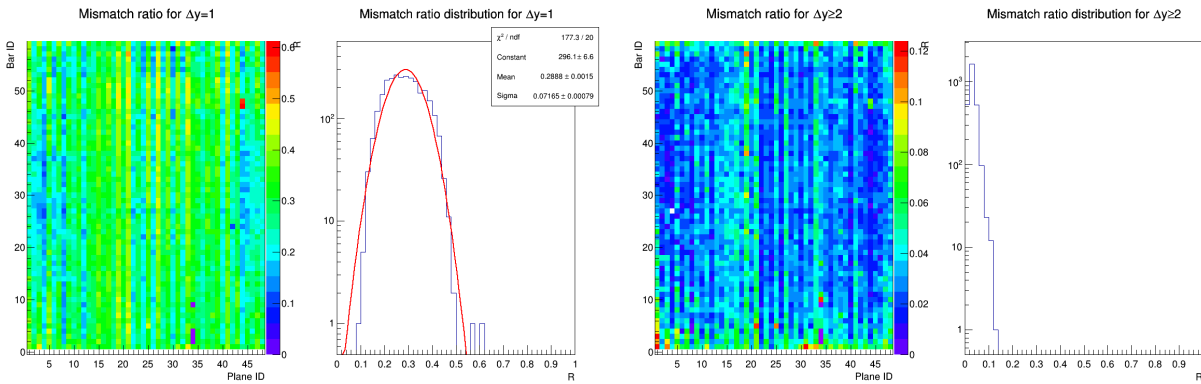


Figure 26: Mismatch ratio for adjacent bars.

Figure 27: Mismatch ratio for distant bars.

The same analysis has been conducted for potential mismatches of two bars or more,  $R_{i \geq 2}$ .

Figure 27 represents the value of that ratio for each channel. The results strongly reject any mismatch at this level.

### 420 3.6 PMT Calibration

A thorough charge calibration was performed shortly after completion of the detector. Cosmic data was used and the charge on the MAPMT side,  $Q_M^i$  was reconstructed by using Equation (1). Provided these measurements, a calibration constant is produced for each MAPMT and SAPMT channel through

$$\epsilon_M^i = \frac{\overline{Q_M^i}}{\frac{1}{N} \sum_i Q_M^i}, \quad \epsilon_S^i = \frac{\overline{Q_S^i}}{\frac{1}{N} \sum_i Q_S^i} \quad (5)$$

$$\epsilon_M^i = \frac{\overline{Q_M^i}}{\frac{1}{N} \sum_{j=1}^N \overline{Q_M^j}}, \quad \epsilon_S^i = \frac{\overline{Q_S^i}}{\frac{1}{N} \sum_{j=1}^N \overline{Q_S^j}} \quad (6)$$

425 with  $\overline{Q}$  the average charges measured in the channel. N is the total number of channels under calibration. The index  $M$  stands for MAPMT and  $S$  stands for SAPMT respectively. Provided calibration, each charge measured is adjusted by dividing it by its corresponding calibration constant.

The measurements obtained for the 5664 channels of the EMR are represented in figure 28. The figure compiles the mean and median charges recorded in the MAPMT and SAPMT for each channel and each plane. These values are used to compile the calibration constants.

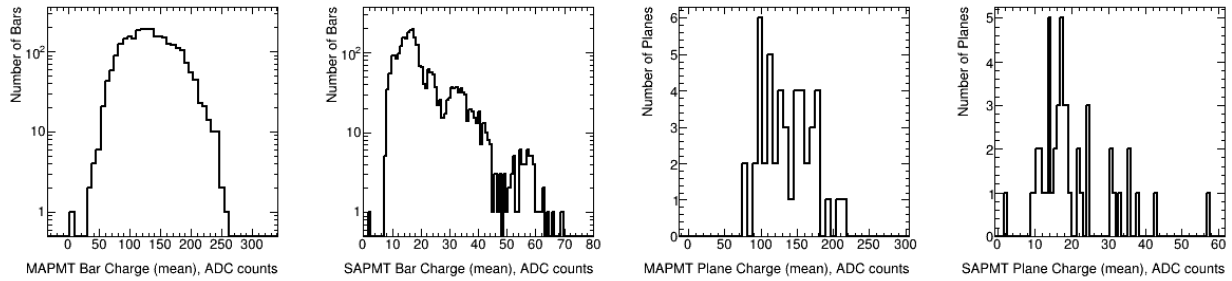


Figure 28: Results of the first round of calibration soon after the EMR was powered on

## 4 Transportation and installation at Rutherford Lab

The total weight of the EMR detector is 2.5 tonnes. Therefore a special care was taken to insure safety and shock-free transportation of the detector. Namely, the detector was attached to special shock absorbers designed to withstand this weight and allow for shock absorption in all three directions. 435 The shock absorbers were then attached to a pallet by which the detector was handled. It was placed in a truck and transported from University of Geneva to Rutherford Lab (Didcot, Oxfordshire, UK) over more than 1100 kilometres.

Once delivered to the Rutherford Lab the EMR detector was installed in the MICE hall and positioned vertically at the end of existing MICE beamline. Later, it was exposed to a beam which 440 parameters were varied in order to achieve different beam compositions and momenta. This data was used to verify the designed functionality of the detector, i.e. the ability to distinguish different particle types (muons, electrons and pions) and to measure their ranges [21].

## Acknowledgement

The work described here was made possible by grants from Swiss National Science Foundation, in the framework of the SCOPES programme and the European Community under the European Commission Framework Programme 7 (AIDA project, grant agreement no. 262025). We gratefully acknowledge all sources of support.

## References

- [1] Mice web site. <http://mice.iit.edu>, contains detailed information about the experiment.
- [2] D. Neuffer. Principles and applications of muon cooling. *Part. Accel.*, 14:75, 1983.
- [3] C. N. Booth et al. The design, construction and performance of the mice target. *Journal of Instrumentation*, 8:P03006, 2013.
- [4] ISIS pulsed neutron and muon source at the Rutherford Appleton laboratory. web site. <http://www.isis.stfc.ac.uk>.
- [5] S. Choubey et al. International design study for the neutrino factory. *Interim Design Report*, IDS-NF-20, 2011. arXiv:hep-ex/1112.2853.
- [6] R. Asfandiyarov. Totally active scintillator tracker-calorimeter for the Muon Ionization Cooling Experiment. *University of Geneva, PhD thesis*, 2014.
- [7] A. Pla-Dalmau, A. Bross, and K. Mellott. Low-cost extruded plastic scintillator. *Nucl. Instrum. Meth.*, A466:482–491, 2001. FERMILAB-PUB-00-177-E.
- [8] A. Pla-Dalmau. Extruded plastic scintillator for the MINOS calorimeters. *Frascati Phys.Ser.*, 21:513–522, 2001. FERMILAB-CONF-00-343.
- [9] A. Pla-Dalmau, A. Bross, V. Rykalin, and B. Wood. Extruded plastic scintillator for MINERvA. *Nuclear Science Symposium Conference Record, IEEE*, 3, 2005. FERMILAB-CONF-05-506-E.
- [10] Saint-Gobain Crystals. Scintillating fiber brochure.
- [11] Kuraray. Plastic scintillating fibers brochure.
- [12] Hamamatsu. Multianode photo-multiplier tubes R5900-00-M64 datasheet.
- [13] M. G. Catanesi et al. [HARP Collaboration]. The HARP detector at the CERN PS. *Nucl. Instr. and Meth.*, (A 571):527, 2007.
- [14] R. Asfandiyarov et al. Selecting philips xp 2972 photomultiplier tubes for the electron muon ranger (emr). *MICE internal note*, 2012. MICE-NOTE-DET-383.
- [15] D. Bolognini et al. Tests of the {MICE} electron muon ranger frontend electronics with a small scale prototype. *Nuclear Instruments and Methods in Physics Research Section A: Accelerators, Spectrometers, Detectors and Associated Equipment*, 646(1):108 – 117, 2011.
- [16] S. Franz and P. Barrillon. Atlas alfa-measuring absolute luminosity with scintillating fibres. *Nuclear Instruments and Methods in Physics Research, Section A: Accelerators, Spectrometers, Detectors and Associated Equipment*, 610(1):35–40, 2009.

- [17] CAEN. V1731 4/8 ch. 8 bit 1000/500 ms/s Digitizer. Technical information manual.
- [18] R. Asfandiyarov, A. Blondel, F. Drielsma, and Y. Karadzhov. Electron-Muon Ranger (EMR)  
480 Electronics Quality Tests. *MICE internal note*, 2014. MICE-NOTE-DET-441.
- [19] R. Asfandiyarov, A. Blondel, F. Drielsma, and Y. Karadzhov. Crosstalk and Misalignment in  
the Electron-Muon Ranger (EMR). *MICE internal note*, 2014. MICE-NOTE-DET-440.
- [20] F. Drielsma. Electron Muon Ranger (EMR) hardware characterization. *University of Geneva,  
Master thesis*, 2014. [http://mice.iit.edu/phd/EMR\\_hardware\\_characterization.pdf](http://mice.iit.edu/phd/EMR_hardware_characterization.pdf).
- 485 [21] D. Adams et al. MICE collaboration. Electron-muon ranger: performance in the mice muon  
beam. *Journal of Instrumentation*, 10:P12012, 2015.